The anisotropic signal of topotaxy during phase transitions in D″

Andrew M. Walker [a,*] David P. Dobson [c] James Wookey [b]
Andy Nowacki [a] Alessandro M. Forte [d]

[a] *School of Earth and Environment, University of Leeds, Leeds, LS2 9JT. UK*

[b] *School of Earth Sciences, University of Bristol, Wills Memorial Building, Queen's Road, Bristol, BS8 1RJ. UK*

[c] *Department of Earth Sciences, University College London, Gower Street, London, WC1E 6BT. UK*

[d] *Department of Geological Sciences, University of Florida, Williamson Hall, P.O. Box 112120, Gainesville, FL 32611, USA*

Abstract

While observations and modelling of seismic anisotropy in the lowermost mantle offers the possibility of imaging mantle flow close to the core-mantle boundary, current models do not explain all observations. Here, we seek to explain a long-wavelength pattern of shear wave anisotropy observed in anisotropic tomography where vertically polarised shear waves travel faster than horizontally polarised shear waves in the central Pacific and under Africa but this pattern is reversed elsewhere. In particular, we test an explanation derived from experiments on analogues, which suggest that texture may be inherited during phase transitions between bridgmanite (perovskite structured $MgSiO_3$) and post-perovskite, and that such texture inheritance may yield the long-wavelength pattern of anisotropy. We find that models that include this effect correlate better with tomographic models than those that assume deformation due to a single phase in the lowermost mantle, supporting the idea that texture inheritance is an important factor in understanding lowermost mantle anisotropy. It is possible that anisotropy could be used to map the post-perovskite stability field in the lowermost mantle, and thus place constraints on the temperature structure above the core-mantle boundary.

Key words: post-perovskite, seismic anisotropy, lowermost mantle, phase transition, mantle convection

* Corresponding author.
Email address: a.walker@leeds.ac.uk (Andrew M. Walker).

Highlights

- Method to include effect of phase transition on anisotropy prediction in D″
- Inclusion of texture inheritance gives switch in anisotropy during phase transition
- Models with texture inheritance give better match to global tomography than single phase models

---

1 Introduction

Recognising patterns of flow in the lowermost mantle (D″) is critical to our understanding of the evolution and dynamics of the Earth. Heat flow through this region is believed to control core cooling, the generation of the Earth's magnetic field and the growth of the inner core, while the related generation of thermal instabilities can lead to the formation of mantle plumes (e.g. Lay et al., 2008). These processes are modified by the arrival of subducted slabs at the core mantle boundary, which are also believed to sculpt heterogeneity concentrated at the base of the mantle into large scale structures (e.g. Garnero et al., 2016). The prospect that observations of seismic anisotropy can be used to probe flow in the deepest mantle has motivated the wide range of seismological, mineralogical and geodynamical studies that are needed to advance this idea and reveal the flow patterns (e.g. McNamara et al., 2002; Panning and Romanowicz, 2004; Hall et al., 2004; Wookey et al., 2005b; Long and Becker, 2010; Nowacki et al., 2011). While measurements of shear wave splitting from ScS, SKS and Sdiff phases unambiguously identify seismic anisotropy in the lowermost mantle (e.g. Lay and Young, 1991; Vinnik et al., 1995; Kendall and Silver, 1996; Wookey et al., 2005a; Rokosky et al., 2006; Long, 2009; He and Long, 2011) and show that in some places the elastic symmetry must be at most orthorhombic (Nowacki et al., 2010; Ford et al., 2015), our most spatially complete observations come from tomographic inversion of global seismic anisotropy where higher symmetry is often assumed.

Anisotropic tomographic models of global shear-wave velocities such as SAW-642AN (Panning and Romanowicz, 2006), S362WMANI (Kustowski et al., 2008), SAW642ANb (Panning et al., 2010), S362WMANI+M (Moulik and Ekström, 2014), and SEMUCB-WM1 (French and Romanowicz, 2014, 2015) assume radial anisotropy compatible with material with hexagonal elastic symmetry and a vertical rotation axis (called vertical transverse isotropy, VTI). While this requires five elastic parameters for a full description, the use of empirical scaling relations reduce the description of shear wave anisotropy to two parameters, such as the velocity of a horizontally propagating shear wave with

horizontal, V_{SH}, and vertical, V_{SV}, polarised particle motion, or a single shear wave velocity and an anisotropic parameter, $\xi = V_{SH}^2/V_{SV}^2$. Even with this simplification, the degree to which anisotropy is resolved in the lowermost mantle is typically lower than the resolution of isotropic inversions and anisotropic tomographic models, using different methods and parameterisations, are in less good agreement with each other at these depths than collections of isotropic models (e.g. Lekić et al., 2012). However, all models have some large scale features in common. In particular, in regions of the lowermost mantle around the central and western Pacific and under southern Africa V_{SV} is faster than V_{SH} while for much of the rest of the lowermost mantle V_{SH} is found to be faster than V_{SV}. This $V_{SH} > V_{SV}$ signal is also observed in the global average (Montagner and Kennett, 1996; de Wit and Trampert, 2015, but see Beghein et al., 2006)

Since the discovery of the phase transition from bridgmanite (perovskite structured $MgSiO_3$) to post-perovskite at conditions similar to those found in the lowermost mantle (Murakami et al., 2004; Oganov and Ono, 2004; Tsuchiya et al., 2004a) much attention has focussed on the ability of the alignment of post-perovskite crystals to explain the observed seismic anisotropy (Lay and Garnero, 2007; Wookey and Kendall, 2007; Nowacki et al., 2011). A key assumption is that flow in the lowermost mantle causes deformation of post-perovskite by the motion of dislocations. This deformation mechanism causes the rotation of the crystal lattices and the creation of a crystallographic (or lattice) preferred orientation (CPO). As single crystals are elastically anisotropic the rock aggregate develops an elastic anisotropy and this is the presumed cause of observed seismic anisotropy. In this case knowledge of the way that dislocations can move in lowermost mantle minerals can, in principle, be used together with seismic observations to infer flow patterns (e.g. Doornbos et al., 1986; Lay and Young, 1991; Karato, 1998a,b; McNamara et al., 2002; Panning and Romanowicz, 2004). In order to use this information to inform models of mantle flow it is necessary to know the elastic anisotropy of single crystal post-perovskite, the deformation mechanism and how this relates strain to the formation of CPO (e.g. knowledge of the critical resolved shear stress for each dislocation slip system, or the stress needed to form deformation twins), and to undertake measurements of seismic anisotropy in the lowermost mantle. However, thus far there have been few attempts to constrain lowermost mantle flow directly from observations of seismic anisotropy (e.g. Wookey et al., 2005a; Wookey and Kendall, 2008; Nowacki et al., 2010; Thomas et al., 2011; Ford et al., 2015).

For post-perovskite in D″, the single crystal elasticity is fairly well constrained from atomic scale simulations (Iitaka et al., 2004; Tsuchiya et al., 2004b; Caracas and Cohen, 2005; Stackhouse et al., 2005; Wentzcovitch et al., 2006; Stackhouse and Brodholt, 2007) and experiments (Murakami et al., 2007; Mao et al., 2010), but consensus on how post-perovskite deforms under lowermost mantle

conditions remains elusive. Because it is only stable at very high pressure, deformation experiments on $MgSiO_3$ post-perovskite are limited to those that can be undertaken in the diamond anvil cell (DAC), which imposes limitations on the range of strains, strain rates, stresses, temperatures and grain sizes that can be investigated. Miyagi et al. (2010) showed that under achievable low-temperature, high-stress conditions deformation yielded a texture consistent with that expected from the movement of dislocations gliding on (001). DAC experiments with the $MnGeO_3$ and $MgGeO_3$ analogues give similar results (Hirose et al., 2010; Nisr et al., 2012). Earlier studies indicating dislocation glide on (100) or {110} (Merkel et al., 2006, 2007) seem to be explained as a transformation texture (see Walte et al., 2009; Okada et al., 2010; Miyagi et al., 2011). Additional information has been extracted from analogue materials with a lower-pressure perovskite to post-perovskite phase transition as deformation can then be undertaken at high temperature and with more control over, for example, strain rate and stress. Such experiments on $CaIrO_3$ and $NaCoF_3$ indicate that post-perovskite is weaker than perovskite (Hunt et al., 2009; Dobson et al., 2012) and that the dominant dislocation slip system for $CaIrO_3$ and $CaPtO_3$ post-perovskite is [100](010) (Yamazaki et al., 2006; Niwa et al., 2007; Walte et al., 2007; Miyagi et al., 2008; Miyajma and Walte, 2009; McCormack et al., 2011; Hunt et al., 2016). This contradicts the results found for $MnGeO_3$ and $MgGeO_3$. An alternative approach to avoid the limitations of DAC experiments is to make use of atomic scale simulation to investigate the way that post-perovskite deforms. Simulations designed to probe atomic diffusion in post-perovskite indicate that diffusion is strongly anisotropic and, if deformation is influenced by atomic diffusion, support the idea that $MgSiO_3$ post-perovskite is weaker than bridgmanite (Ammann et al., 2010). Models of dislocation mobility within the Peierls-Nabarro framework suggest that deformation of $MgSiO_3$ post-perovskite in the dislocation controlled regime should be dominated by motion of dislocations belonging to the [100](010) and [001](010) slip systems (Carrez et al., 2007a,b), that $CaIrO_3$ should behave in a similar manner to $MgSiO_3$ but not $MgGeO_3$ (Metsue et al., 2009) and that the addition of Fe does should not dramatically alter this behaviour (Metsue and Tsuchiya, 2013). Recent calculations going beyond the Peierls-Nabarro approximations and incorporating thermal effects reinforce the importance of the [100](010) slip system in $MgSiO_3$ post-perovskite (Goryaeva et al., 2015a,b) and suggest the possibility of dislocation accommodated anelasticity (Goryaeva et al., 2016). As yet, the apparent disagreement between the DAC experiments, studies of analogues, and simulations remains unresolved.

There have been several attempts to use geodynamical modelling alongside simulations of the development of anisotropy parameterised by data from mineral physics to understand shear-wave splitting or long-wavelength anisotropy (e.g. Wenk et al., 2006, 2011; Walker et al., 2011; Nowacki et al., 2013; Cottaar et al., 2014) and place inferences of mantle flow derived from observations of

anisotropy on a stronger footing. The main differences between these studies are: (a) the choice of how to generate a mantle flow field that drives deformation, either by 2D (Wenk et al., 2006, 2011) or 3D (Cottaar et al., 2014) simulations of convection, or by using flow field generated by the inversion of geophysical observations (Walker et al., 2011; Nowacki et al., 2013); (b) whether they seek to compare predictions with observations of shear wave splitting making use of a ray theoretical calculation (Nowacki et al., 2013), with summary anisotropic parameters more comparable with tomography (Wenk et al., 2011; Walker et al., 2011), or both (Cottaar et al., 2014); and (c) the details of the model of texture evolution in post-perovskite or other deep mantle phases. Studies based on mantle flow derived from geophysical observation are set in the geographical reference frame of the Earth, and this allows a relatively direct comparison with observations of anisotropy. However, such approaches make use of models of mantle flow that are damped and are at relatively low spatial resolution: this may modify deformation experienced by rocks in the deep mantle. A further limitation is that such models do not vary with time. These limitations are not present when a forward simulation of mantle flow is used, which yield a time varying flow field at a spatial resolution only limited by the available computational resources, but at the cost of losing the ability to directly compare such models with specific geolocated observations. Comparison with shear wave splitting (e.g. Nowacki et al., 2013; Cottaar et al., 2014) is generally limited to regions close to the location where subducting slabs are expected to impinge on the core-mantle boundary (although Ford et al., 2015, combined observations of ScS and SK(K)S to explore anisotropy around the African LLSVP) and these studies tend to yield evidence for anisotropy consistent with post-perovskite deformation with glide on (010) or (001). However, an important caveat derived from recent finite-frequency simulation is that these ray-theoretical approaches may be inaccurate if lowermost mantle anisotropy is complex and spatially varying (Nowacki and Wookey, 2016). In contrast with the studies of shear wave splitting, results from comparison with global tomography are less easily explained. In particular, the low-degree pattern with large areas of $V_{SV} > V_{SH}$ in the central Pacific and under Africa and $V_{SH} > V_{SV}$ elsewhere is hard to explain when the anisotropy is generated by a single mechanism. Wenk et al. (2011) suggest that the $V_{SV} > V_{SH}$ areas may represent upwelling, while Walker et al. (2011) suggest that these areas may represent the regions of maximum strain at the end of long pathlines (invoking slip systems for post-perovskite that were different to those preferred by Wenk et al., 2011). Resolving the origin of this long wavelength feature of lowermost mantle anisotropy is an important step in attempts to understand flow in the deepest mantle.

A possible explanation for the long wavelength anisotropic structure of D″ was recently proposed by Dobson et al. (2013) following experiments on the $NaNiF_3$ analogue of $MgSiO_3$ post-perovskite (Dobson et al., 2011). $NaNiF_3$ perovskite was annealed in the post-perovskite stability field and partially

transformed crystals recovered to ambient conditions. These crystals maintained the morphology of the perovskite crystals but contained lamellae of post-perovskite. A combination of single-crystal X-ray diffraction, transmission electron microscopy, and electron diffraction demonstrated that the orientations of the crystal lattices of the un-transformed perovskite and new post-perovskite lamellae were consistently related. These topotactic relations provide strong evidence for a martensitic transformation mechanism where any deformation induced CPO can be inherited during the phase transition. This finding is consistent with the results of previous experimental (Tschauner et al., 2008; Okada et al., 2010; Miyagi et al., 2011) and computational (Oganov et al., 2005; Zahn, 2011, 2013) studies. By considering simple shear parallel to the CMB, Dobson et al. (2013) demonstrated that deformation of post-perovskite followed by a temperature induced transformation to bridgmanite and further deformation in the perovskite stability field is broadly consistent with the pattern of anisotropy revealed by global anisotropic tomography. Here we extend this analysis by considering a more realistic three-dimensional flow and deformation field in the lower mantle and investigate the possibility that the long wavelength pattern of lowermost mantle anisotropy provides evidence for texture inheritance in the lowermost mantle.

2 Methods

Our basic approach follows that of Walker et al. (2011) in that particles are tracked along pathlines integrated through a mantle flow model that is itself derived from an inversion of geophysical observations. The strain imposed on these particles is calculated from the mantle flow model and used to drive simulations of texture development. We have modified this approach to account for deformation in the bridgmanite stability field and for topotaxy in the bridgmanite to post-perovskite and post-perovskite to bridgmanite phase transitions. In common with Walker et al. (2011), we use fourth-order Runge-Kutta integration to trace pathlines backwards through a steady state flow field and numerical differentiation at each time step to find the velocity gradient tensors describing macroscopic deformation of the mantle. The velocity gradient tensors are then used together with a description of the slip-system properties of lower-mantle minerals to drive simulations of CPO formation using the visco-plastic self consistent (VPSC: Lebensohn and Tomé, 1993) approach. We use the same choice of parameters and software as Walker et al. (2011) with consideration of 500 grains, the tangent linearisation scheme, no slip system hardening caused by strain, and version 7c of the VPSC implementation from Los Alamos National Laboratory. The calculated CPO at the end of each pathline are combined with descriptions of single crystal elasticity in order to evaluate the elastic and seismic anisotropy at each point of interest.

Table 1
Relative slip system critical resolved shear stresses (CRSS) used for VPSC calculations. For post-perovskite, plasticity model P100 uses the parameters of Merkel et al. (2007) which favour slip on the {011} and (100) planes. P010 is taken from the Peierls-Nabarro modelling of Carrez et al. (2007a,b) and Metsue et al. (2009) and favours slip on the (010) plane. P001 is intended to favour slip on the (001) slip as observed by Miyagi et al. (2010). The PV plasticity model for bridgmanite is taken from the simulations reported by Mainprice et al. (2008) at 100 GPa, the highest pressure considered in that study. Slip systems with infinite CRSS cannot accommodate strain.

Slip system	P100	P010	P001	PV
[100](001)	10	2.6	1	2.5
[010](001)	10	4.1	1	1.0
[001](010)	∞	1.0	∞	1.6
[001](100)	2	5.4	10	3.8
[010](100)	1	5.2	10	1.0
[001]{110}	4	2.9	10	1.9
$\langle 110 \rangle$(001)	10	4.1	2	1.8
[100]{011}	∞	6.8	∞	∞
[100](010)	∞	4.7	∞	1.8
$\langle 110 \rangle${110}	1	8.8	10	2.0

In the current work we make use of the same choice of three sets of slip system parameters described in Walker et al. (2011) to simulate the deformation of post-perovskite (we call these 'P100', 'P010' and 'P001'). For bridgmanite we use parameters of Mainprice et al. (2008), which were derived from atomic scale simulation at 100 GPa. We call these parameters 'PV' and note that the weakest predicted slip system is [010](100) not [001](100) as inferred by recent experiments at 25 GPa and 1873 K (Tsujino et al., 2016). This difference may be due to the effect of temperature, which thus far has only been considered for [100](010) and [010](100) in bridgmanite (Kraych et al., 2016a,b). All slip system parameters are given in Table 1. For consistency with Walker et al. (2011) we use the same interpolative approach described in Ammann et al. (2010) to generate single crystal elastic constants at the pressure and temperature of interest using values and derivatives from density functional theory for post-perovskite (Stackhouse et al., 2005; Wentzcovitch et al., 2006; Stackhouse and Brodholt, 2007) and bridgmanite (Oganov et al., 2001; Wentzcovitch et al., 2004) and combine these with the CPO to define the Voigt-Reuss-Hill mean elasticity of the aggregate.

The mantle flow model is based on the TX2008 global tomography model

that describes both mantle density and shear-velocity anomalies derived from a joint inversion of S-wave travel times, core mantle boundary ellipticity, dynamic surface topography and the gravity field (Simmons et al., 2009). The tomographically inferred 3-D distribution of mantle density anomalies is combined with the 'V2' mantle viscosity profile of Forte et al. (2010), in a theory of viscous flow in a compressible, self-gravitating spherical mantle coupled to surface place motions. This flow calculation and the results are presented in Forte et al. (2015). The temperature anomalies derived from the TX2008 tomography model are employed in the calculation of the single crystal elasticities and to define the location of the bridgmanite to post-perovskite phase transition. This is found by using the temperature anomalies to perturb the one-dimensional geotherm of Stacey and Davis (2008) as described in Ammann et al. (2014). The phase boundary is assumed linear in pressure-temperature space and a slope and zero-kelvin intercept of 9.6 MPa/K and 98.7 GPa are used (Oganov and Ono, 2004). This simple model of the phase boundary serves to illustrate the effect of the phase transition on anisotropy in D″, but we note that there is significant uncertainty on its location and on how it may move with changes in composition (Murakami et al., 2005; Hirose et al., 2005; Hirose, 2006; Catalli et al., 2009; Grocholski et al., 2012). Furthermore, there is a trade-off between the parameters used to describe the temperature structure of the lowermost mantle and those used to locate the phase boundary. This is discussed further below. In Walker et al. (2011) this led to two stopping conditions for particle tracing (and two initial conditions for the models of texture development). The first is to ignore topography on the phase boundary and imagine that constant thickness layer of post-perovskite exists at the base of the mantle. In this case particle tracing stops 150 km above the CMB and the VPSC simulation is run forward from here starting from a post-perovskite aggregate with a uniform random CPO. The second stop condition respects topography on the phase boundary and traces particles back as far as the first crossing of the phase boundary. A uniform random CPO is again used to start the VPSC simulation. It is notable that in this case no information on the anisotropy in locations where bridgmanite is the stable phase could be provided.

2.1 Modeling texture inheritance

Our model of texture inheritance builds on the second 'topographic' stop condition used in Walker et al. (2011) and extends this by allowing pathlines to pass freely between the two phase stability regions. We segment each pathline each time it passes from the bridgmanite to post-perovskite or from the post-perovskite to bridgmanite stability field and then run a VPSC simulation for each segment in turn, transferring the texture from the end of one segment to the start of the next. Two changes are needed when switching from one

segment to another. First, the slip system parameters and description of the crystallography must be updated. Second, as outlined below, the output texture must be modified before being used as input for the new calculation. This approach permits us to calculate the anisotropy within the bridgmanite and post-perovskite stability fields in any chosen location.

The texture modification procedure is designed to reproduce the relationship between perovskite and post-perovskite orientations in $NaNiF_3$ found by Dobson et al. (2013). In these experiments the c-axis of perovskite was found to be parallel with the c-axis of post-perovskite and the b-axis in perovskite was found to be perpendicular to (110) in post-perovskite. The relationship between the two crystal lattices can thus be described as a rotation about their common c-axis. In order to transform the texture, we define unit vectors with respect to the orientation of a post-perovskite crystal aligned along its a-, b- and c-axes ($\hat{a}_{\mathrm{PPv}}$, $\hat{b}_{\mathrm{PPv}}$ and $\hat{c}_{\mathrm{PPv}}$, respectively), along the $[\bar{1}10]$ and $[1\bar{1}0]$ directions ($\hat{d}_{[\bar{1}10]_{\mathrm{PPv}}}$, $\hat{d}_{[1\bar{1}0]_{\mathrm{PPv}}}$), and normal to (110), $\hat{g}_{110_{\mathrm{PPv}}}$. The rotation associated with the post-perovskite to perovskite ($NaNiF_3$ or bridgmanite) phase transition is then described by a rotation matrix formed of the dot products of vectors along the crystallographic directions before and after the transformation:

$$\mathbf{g}_{\mathrm{PPv}^{(a)}\rightarrow\mathrm{Pv}} = \begin{bmatrix} \hat{a}_{\mathrm{PPv}} \cdot \hat{d}_{[1\bar{1}0]_{\mathrm{PPv}}} & \hat{b}_{\mathrm{PPv}} \cdot \hat{d}_{[1\bar{1}0]_{\mathrm{PPv}}} & 0 \\ \hat{a}_{\mathrm{PPv}} \cdot \hat{g}_{110_{\mathrm{PPv}}} & \hat{b}_{\mathrm{PPv}} \cdot \hat{g}_{110_{\mathrm{PPv}}} & 0 \\ 0 & 0 & 1 \end{bmatrix}. \tag{1}$$

Dobson et al. (2013) also found that a second post-perovskite orientation was possible and that post-perovskite formed twins during the transformation. The rotation matrix associated with the second orientation is given by:

$$\mathbf{g}_{\mathrm{PPv}^{(b)}\rightarrow\mathrm{Pv}} = \begin{bmatrix} \hat{a}_{\mathrm{PPv}} \cdot \hat{d}_{[\bar{1}10]_{\mathrm{PPv}}} & \hat{b}_{\mathrm{PPv}} \cdot \hat{d}_{[\bar{1}10]_{\mathrm{PPv}}} & 0 \\ \hat{a}_{\mathrm{PPv}} \cdot \hat{g}_{110_{\mathrm{PPv}}} & \hat{b}_{\mathrm{PPv}} \cdot \hat{g}_{110_{\mathrm{PPv}}} & 0 \\ 0 & 0 & -1 \end{bmatrix}. \tag{2}$$

We note that transformations in the opposite sense, from perovskite to post-perovskite, are described by the transpose of these two rotation matrices (i.e. $\mathbf{g}_{\mathrm{Pv}\rightarrow\mathrm{PPv}^{(a)}} = \mathbf{g}^{\mathrm{T}}_{\mathrm{PPv}^{(a)}\rightarrow\mathrm{Pv}}$ and $\mathbf{g}_{\mathrm{Pv}\rightarrow\mathrm{PPv}^{(b)}} = \mathbf{g}^{\mathrm{T}}_{\mathrm{PPv}^{(b)}\rightarrow\mathrm{Pv}}$). In order to implement the transformation from one one phase to the other, we convert the representation of each crystal orientation at the end of the previous segment of the pathline from Euler angles to a rotation matrix, $\mathbf{g}^n$, add the rotation from perovskite to post-perovskite (or vice versa), then transform the resulting orientation back to Euler angles to generate a texture for the start of the next segment of the pathline. For each crystal, we randomly select between the two orientations with equal probability. The orientations of post-perovksite, crystals, $\mathbf{g}_{\mathrm{PPv}}$, following a transformation from perovskite (with crystal orien-

tations denoted as $\mathbf{g}_{\mathrm{Pv}}$) is given by:

$$\mathbf{g}^n_{\mathrm{PPv}} = \begin{cases} \mathbf{g}^n_{\mathrm{Pv}} \times \mathbf{g}_{\mathrm{Pv}^{(a)}\rightarrow\mathrm{PPv}} & 50\% \text{ chance} \\ \mathbf{g}^n_{\mathrm{Pv}} \times \mathbf{g}_{\mathrm{Pv}^{(b)}\rightarrow\mathrm{PPv}} & 50\% \text{ chance.} \end{cases} \tag{3}$$

Similarly, the orientation of perovskite crystals following transformation from post-perovskite is given by:

$$\mathbf{g}^n_{\mathrm{Pv}} = \begin{cases} \mathbf{g}^n_{\mathrm{PPv}} \times \mathbf{g}_{\mathrm{PPv}^{(a)}\rightarrow\mathrm{Pv}} & 50\% \text{ chance} \\ \mathbf{g}^n_{\mathrm{PPv}} \times \mathbf{g}_{\mathrm{PPv}^{(b)}\rightarrow\mathrm{Pv}} & 50\% \text{ chance.} \end{cases} \tag{4}$$

We note that each $\mathbf{g}^n_{\mathrm{Pv}}$ or $\mathbf{g}^n_{\mathrm{PPv}}$, and the associated set of Euler angles, describe the rotation needed to move a right handed orthogonal coordinate system from an alignment parallel with a global refeence frame, to one aligned with the crystallographic axes of the n^{th} crystal. An implementation of this approach can be found as an example distributed with MSAT (Walker and Wookey, 2012). It may be possible that stress results in a preference for one twin or the other meaning that a probability other than 50% should be used. While this would strengthen the texture immediately following a phase transition we do not consider this as the relationship between the stress tensor and the preference for one orientation or the other is not clear. Another possibility is that some crystals of the new phase form by a nucleation and growth process, which would weaken the initial texture after the phase transition. By assuming 100% "memory" during the phase transition we maximise the likely effect on seismic anisotropy and the difference between models with texture inheritance and those without.

This approach to texture inheritance yields two new stop criteria for pathline tracing (and two corresponding initial conditions for the calculation of texture development), which we compare in order to quantify the importance of texture development in the bulk of the lower mantle on D″ anisotropy. The first of these traces particles backwards to the first bridgmanite to post-perovskite phase transition that the particle experiences during its time in the lower mantle and the texture development process is started from a uniform random orientation distribution at this point. In this approach we assume that previous deformation in the bridgmanite field does not lead to the development of a strong texture, or that any such texture is destroyed during the first phase transition, but that texture is inherited during subsequent back transformation from post-perovskite to bridgmanite (and through any subsequent phase transitions). In practice we need to find some way to decide which phase transition is the first. Our criteria for this is to stop looking for a further phase transition when a particle is more that 450 km above the CMB and is in the bridgmanite stability field. When these conditions are met we discard the current pathline segment and initialise the VPSC simulation from the first bridgmanite to post-perovskite phase transition.

The opposite extreme, and our second initial condition for texture development, is to permit the generation of texture in the lower mantle before a particle first crosses the bridgmanite to post-perovskite phase boundary. We implement this possibility by tracing particles back until they reach a depth of 2000 km (891 km above the CMB), and starting the VPSC simulation with bridgmanite crystals with a uniform random orientation distribution. This depth was chosen to yield significant texture in the bridgmanite stability field as a particle approaches the phase boundary while limiting the maximum pathline length. Although this approach means that the lower mantle above D″ will be seismically anisotropic, we do not attempt to interpret these predictions in terms of anisotropy of the bulk of the lower mantle. Further models evaluated at shallower depths would be needed to compare our simulations with the recent suggestion based on one-dimensional models that the bulk of the lower mantle may be seismically anisotropic (de Wit and Trampert, 2015). Comparing results from these two kinds of model allows us to evaluate the importance of flow in the bulk of the lower mantle on the seismic anisotropy in the lowermost mantle.

A summary of the methodology is shown in Figure 1 and the model naming convention is described in Table 2. We run each model (a combination of one of the two stop criteria, with one of the three sets of parameters describing slip systems in post-perovskite) to evaluate the elastic anisotropy at points 75 and 175 km above the CMB on a $5^\circ \times 5^\circ$ grid in latitude and longitude. These elastic constants are reported in the supplementary information. In order to compare the general anisotropy generated by this method with the VTI anisotropy recovered from global tomography, we then impose hexagonal symmetry with a vertical rotation axis on the elasticity calculated at each point, evaluate the phase velocity of the two polarisation directions for a horizontally propagating ray, and use these to calculate ξ. We then compare the models with each other and with a selection of S-wave models of anisotropy in the Earth.

3 Results

In Figures 2, 3 and 4 we compare the anisotropy predicted from models including texture inheritance with the two stop criteria with results from Walker et al. (2011) assuming a constant thickness layer of post-perovskite using the same flow field for each of the three models of post-perovskite deformation. For all three deformation models the addition of texture inheritance leads to significant changes in the long-wavelength pattern of anisotropy. In the case of the P100 and P010 models (Figures 2 and 3, respectively) the tendency is to remove much of the strong V_{SV} fast signal from regions with long path lengths in D″ and replace this with a relatively weak V_{SH} fast signal inside the bridgmanite stability field. For these plasticity models, the addition of texture

Table 2
List of model names. The various models presented in this paper are described by the concatenation of terms describing the post-perovskite slip system parameters (see Table 1) and and the model used for texture inheritance. Each term used to build a model name is included in the table. For example, the model P001.ttax involves post-perovskite deformation with [010](001) set to the weakest slip system, texture inheritance during phase transitions, but no texturing in the bulk of the lower mantle. File names in the Supplementary Information include "TX2008.V2.T." prepended to the description below to follow the naming convention introduced in Walker et al. (2011), where different mantle flow fields were also considered and some models did not include topography on the phase boundary.

Term	Description
P100	Plasticity model favours slip on {011} and (100)
P010	Plasticity model favours slip on (010)
P001	Plasticity model favours slip on (001)
-	Where no texture inheritance model is indicated the texture is assumed to be reset at each phase boundary
ttax	Texture in inherited through phase transitions, but a uniform random distribution is assumed when the pathline first enters the post-perovskite stability field
pretex	Texture in inherited as described in "ttax", deformation induced texturing of bridgmanite in the bulk of the lower mantle is permitted and this is inherited when the pathline first enters the post-perovskite stability field

inheritance does not improve agreement with the long-wavelength pattern of anisotropy as revealed by seismic tomography. In contrast, the addition of texture inheritance to models based on the P001 slip system parameters leads to patches of V_{SV} fast inside the bridgmanite stability field reversing the tendency for this model to yield strong V_{SH} fast anisotropy where path lengths in D″ are long.

As shown in Figure 5, models of lowermost mantle anisotropy derived from seismic tomography exhibit different resolutions from each other, and from our computed maps of anisotropy, but the general tendency for $V_{SV} > V_{SH}$ under Africa and the Pacific, and $V_{SH} > V_{SV}$ for much of the rest of the lowermost mantle is apparent in all models. It is this feature that we argue can be attributed to texture inheritance. In order to compare our computed models with the results of seismic tomography on a more quantitative basis we fit spherical harmonic coefficients to the models and the tomographic results up to degree-8 and perform degree-by-degree correlation between the models and the tomography (e.g. Eckhardt, 1984; Ray and Anderson, 1994). The resulting comparisons between tomographic models, and each of our nine computed models of anisotropy are shown in Figure 6 along with a global estimate

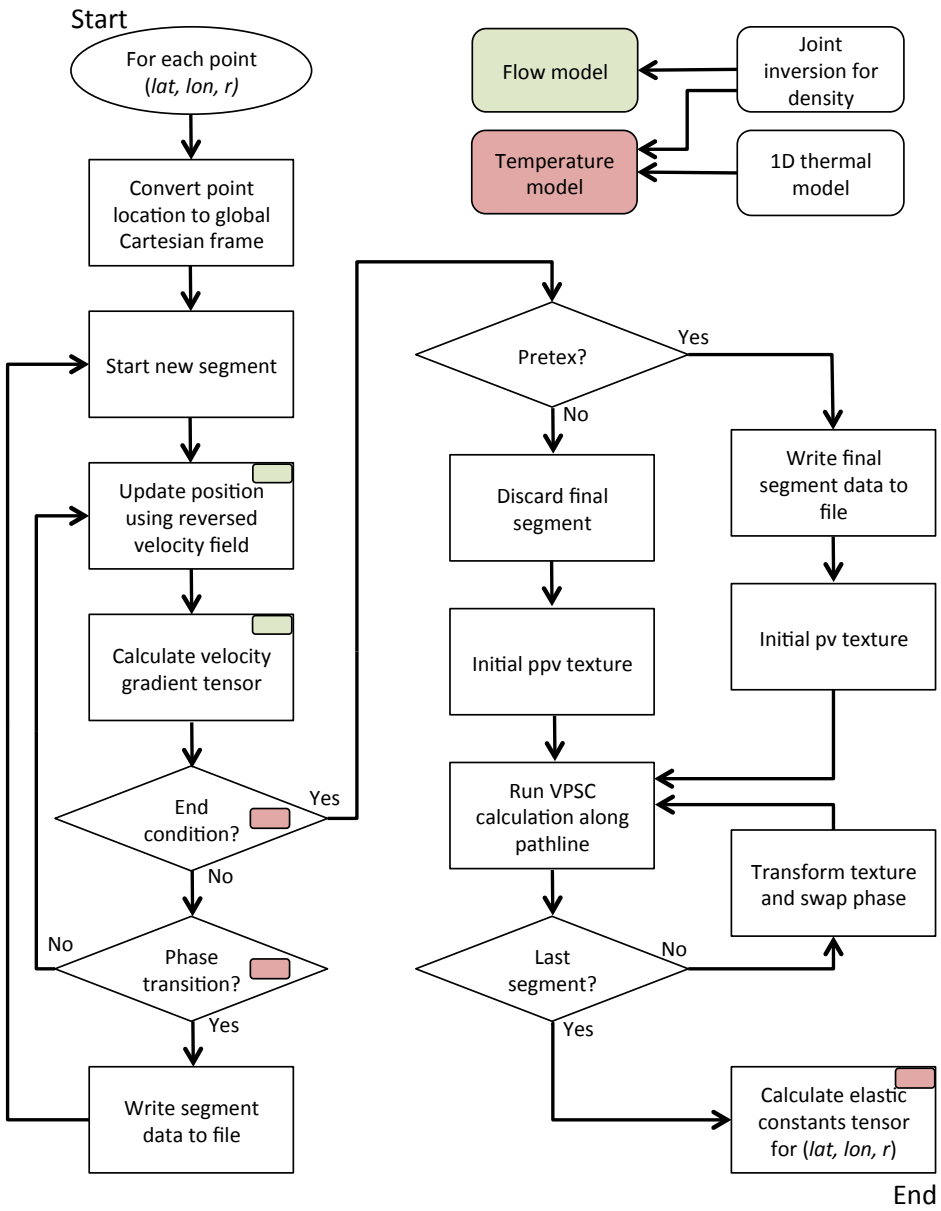

Fig. 1. Steps taken to calculate elastic anisotropy at a point (lat, lon, r) in the lowermost mantle. Use of temperature and flow fields are indicated by coloured boxes. Segments run backwards in time on the left hand side where the pathlines are constructed, but forwards on the right hand side where the VSPC calculations are run. Pathline data for each segment is written in forward order.

of the correlation between models based on a point-by-point comparison the calculation of the linear correlation coefficents. None of our models are particularly strongly correlated with the tomographic results, but by the same measure the tomographic models are not always strongly correlated with each other. Indeed, many of our models are anti-correlated with the tomography on the basis of both the degree-by-degree and point-by-point comparisons and it

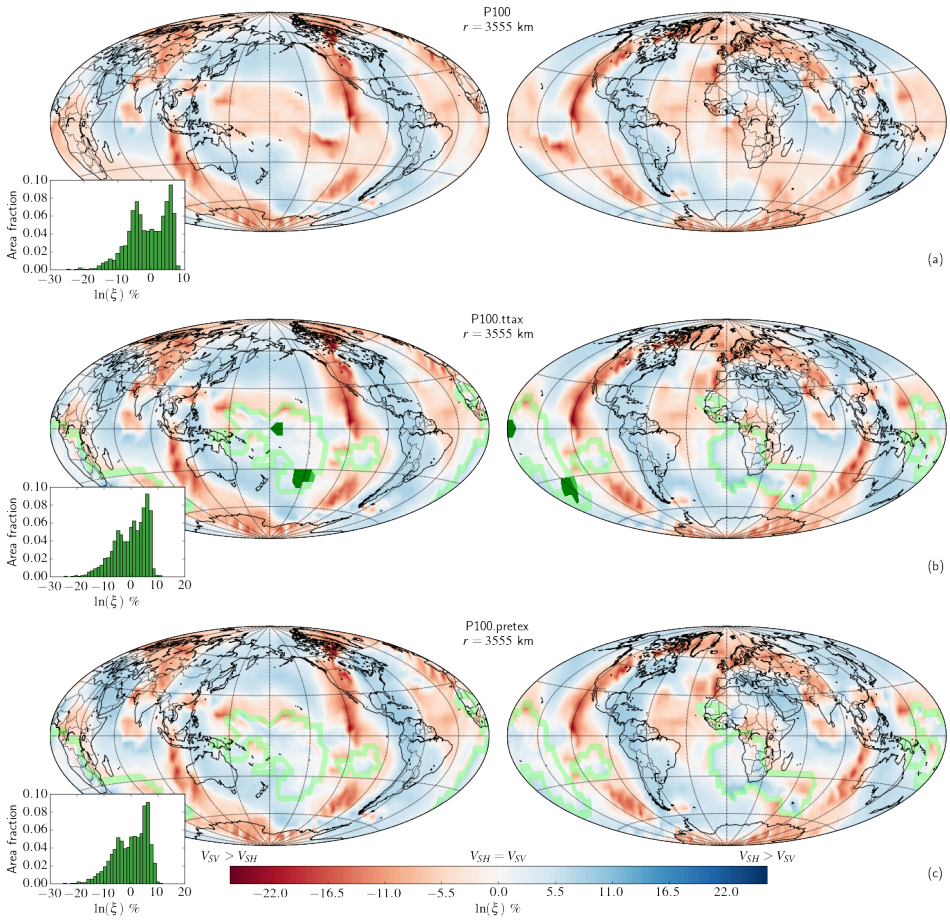

Fig. 2. Calculated anisotropy, expressed as $\ln(\xi)$, 75 km above the core mantle boundary assuming post-perovskite deformation dominated by dislocations gliding on (100) and {110} for three cases described in the main text. (a) Reference case of a 150 km thick layer of post-perovskite from Walker et al. (2011). (b) Mixed post-perovskite and bridgmanite with texture inheritance during the phase transition but starting from an isotropic post-perovskite aggregate. (c) Mixed post-perovskite and bridgmanite with texture inheritance and the development of texture during deformation in the lower mantle prior to the first bridgmanite to post-perovskite phase transition. The light green lines in (b) and (c) outline the phase transition at this depth while dark green patches in (b) show small regions where pathlines end in a region where bridgmanite is stable having never crossed the phase boundary. Inset histograms show the distribution of anisotropy by area. The model naming convention is described in Table 2.

seems reasonable to discount these models of lowermost mantle deformation. Overall, the best match between the tomography and our models appears to be for the models that invoke deformation of post-perovskite dominated by glide on (001) and texture inheritance through the post-perovskite to bridgmanite phase transition. While this does not result in a pattern of anisotropy that fully matches the results of seismic tomography, these models are consistently correlated with the tomography and show good correlation at low spherical

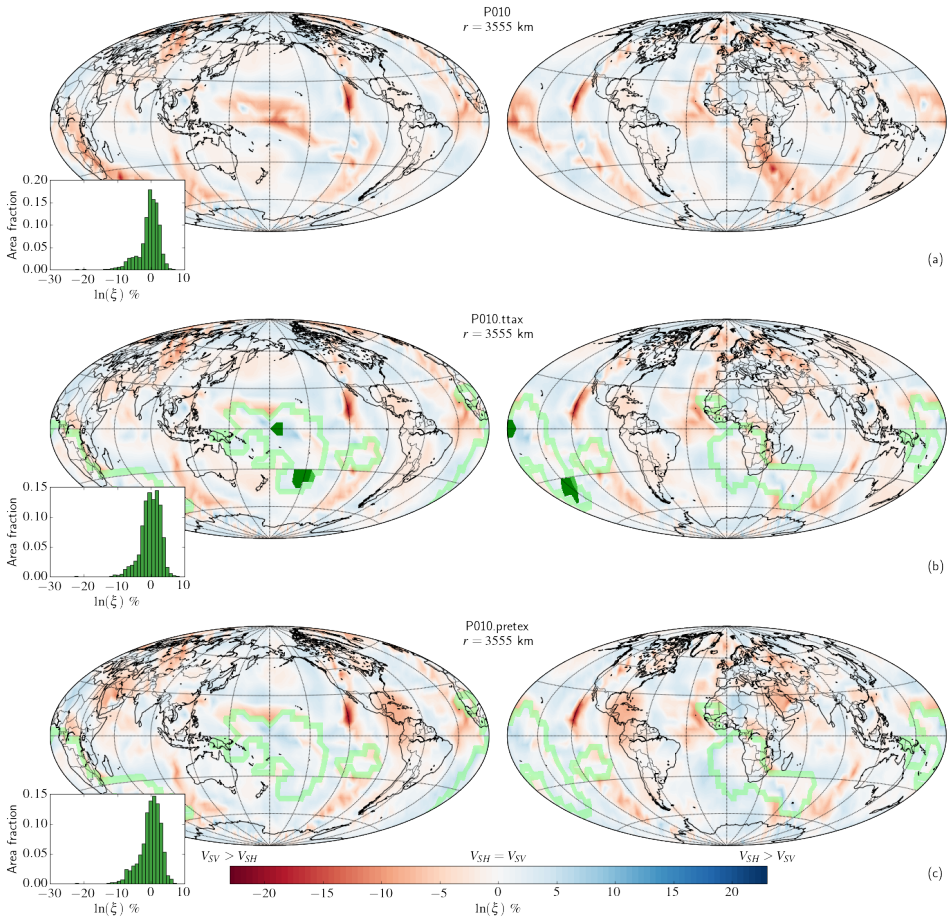

Fig. 3. Same as Figure 2 but assuming post-perovskite deformation is dominated by dislocations gliding on (010).

harmonic degree. Potential modifications to our model that may be expected to further improve the match are described later.

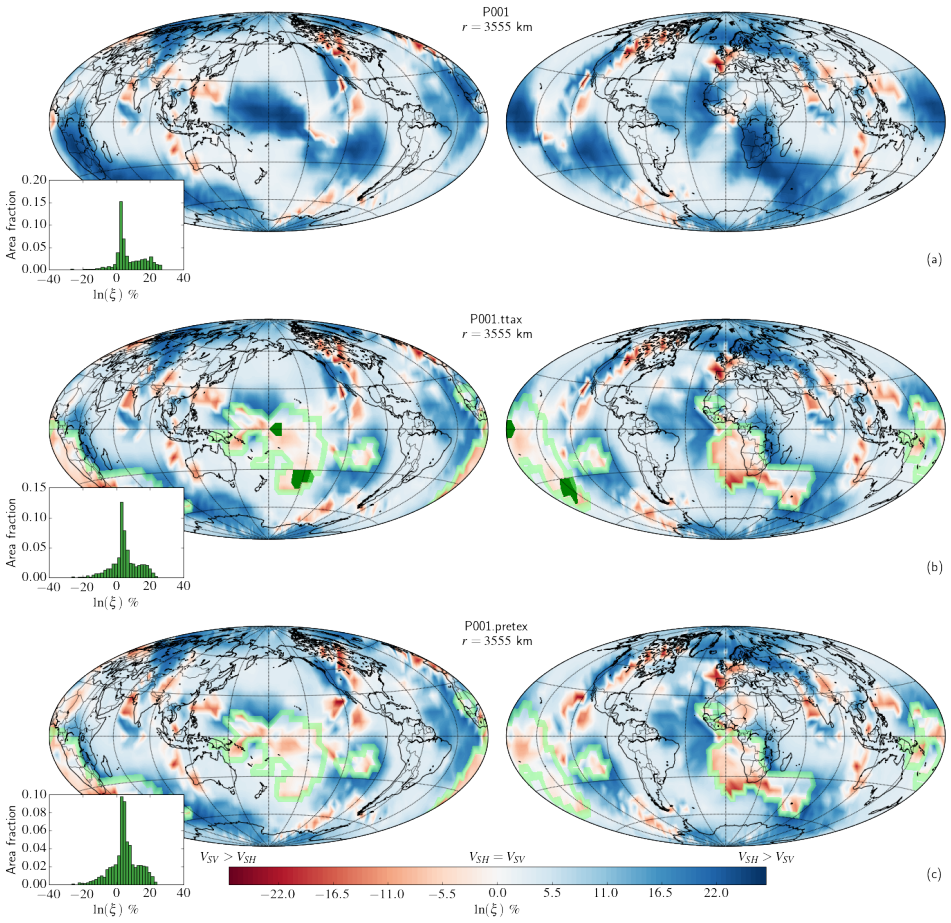

Fig. 4. Same as Figure 2 but assuming post-perovskite deformation is dominated by dislocations gliding on (001).

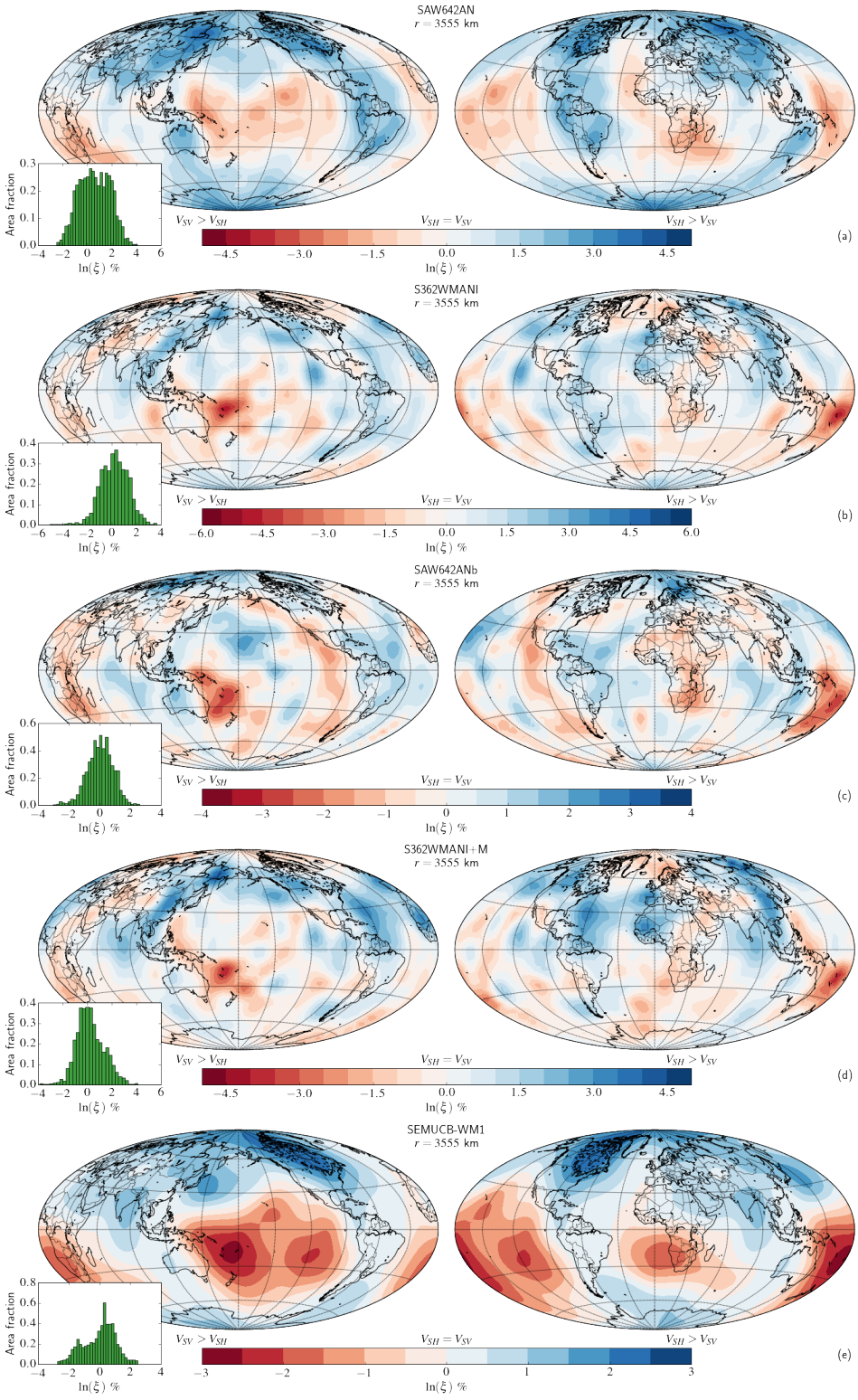

Fig. 5. Anisotropy derived from S-wave tomography 75 km above the CMB. (a) SAW642AN (Panning and Romanowicz, 2006) (b) S362WMANI (Kustowski et al., 2008), (c) SAW642ANb (Panning et al., 2010), (d) S362WMANI+M (Moulik and Ekström, 2014), (e) SEMUCB-WM1 (French and Romanowicz, 2014, 2015)

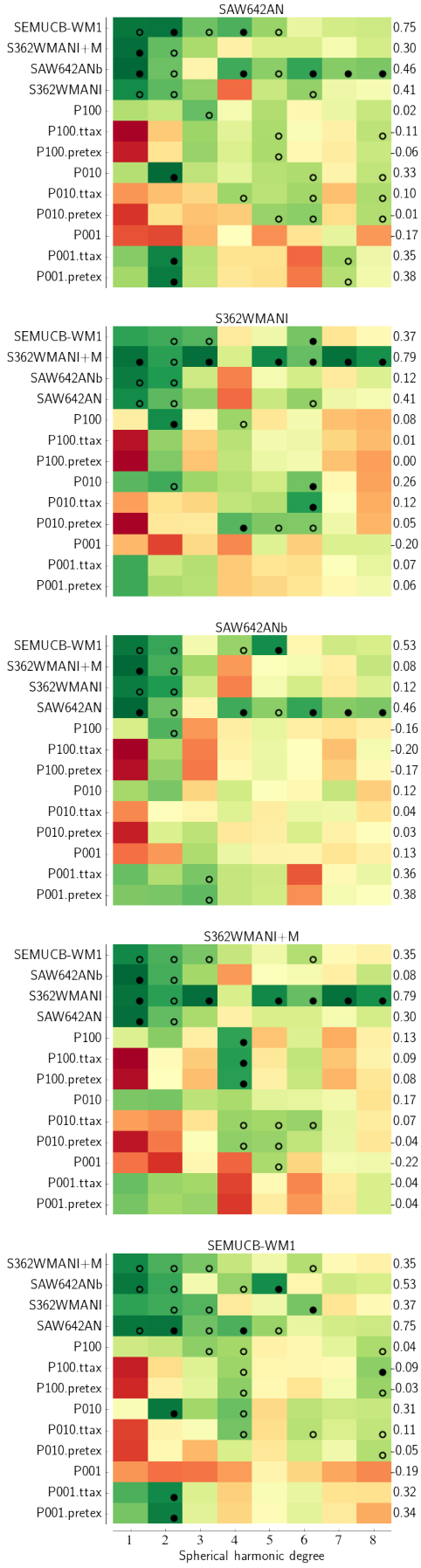
SAW642AN
SEMUCB-WM1 0.75
S362WMANI+M 0.30
SAW642ANb 0.46
S362WMANI 0.41
P100 0.02
P100.ttax -0.11
P100.pretex -0.06
P010 0.33
P010.ttax 0.10
P010.pretex -0.01
P001 -0.17
P001.ttax 0.35
P001.pretex 0.38
S362WMANI
SEMUCB-WM1 0.37
S362WMANI+M 0.79
SAW642ANb 0.12
SAW642AN 0.41
P100 0.08
P100.ttax 0.01
P100.pretex 0.00
P010 0.26
P010.ttax 0.12
P010.pretex 0.05
P001 -0.20
P001.ttax 0.07
P001.pretex 0.06
SAW642ANb
SEMUCB-WM1 0.53
S362WMANI+M 0.08
S362WMANI 0.12
SAW642AN 0.46
P100 -0.16
P100.ttax -0.20
P100.pretex -0.17
P010 0.12
P010.ttax 0.04
P010.pretex 0.03
P001 0.13
P001.ttax 0.36
P001.pretex 0.38
S362WMANI+M
SEMUCB-WM1 0.35
SAW642ANb 0.08
S362WMANI 0.79
SAW642AN 0.30
P100 0.13
P100.ttax 0.09
P100.pretex 0.08
P010 0.17
P010.ttax 0.07
P010.pretex -0.04
P001 -0.22
P001.ttax -0.04
P001.pretex -0.04
SEMUCB-WM1
S362WMANI+M 0.35
SAW642ANb 0.53
S362WMANI 0.37
SAW642AN 0.75
P100 0.04
P100.ttax -0.09
P100.pretex -0.03
P010 0.31
P010.ttax 0.11
P010.pretex -0.05
P001 -0.19
P001.ttax 0.32
P001.pretex 0.34
1 2 3 4 5 6 7 8
Spherical harmonic degree

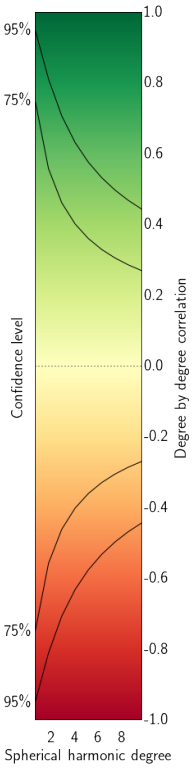
95%
75%
75%
95%
Confidence level
1.0
0.8
0.6
0.4
0.2
0.0
-0.2
-0.4
-0.6
-0.8
-1.0
Degree by degree correlation
2 4 6 8
Spherical harmonic degree

Fig. 6: Degree by degree correlation comparing the five tomographic models shown in Figure 5 with the nine models derived from mantle flow and shown in Figures 2, 3, and 4, all evaluated 75 km above the CMB. A correlation of 1 indicates complete correlation at the particular spherical harmonic degree, 0 shows no correlation, and -1 is anti-correlated. The confidence that can be assigned to any given correlation is dependent on the spherical harmonic degree as shown by lines in the legend. Positive correlation at > 95 % and > 75 % confidence is highlighted by filled and open circles, respectively. The model naming convention (used on the left hand side of each block of correlation coefficients) is described in Table 2. Tomographic models are described by a short acronym; SAW642AN: Panning and Romanowicz (2006), S362WMANI: Kustowski et al. (2008), SAW642ANb: Panning et al. (2010), S362WMANI+M: Moulik and Ekström (2014) SEMUCB-WM1: French and Romanowicz (2014, 2015). Numbers on the right hand side of each block of correlation coefficients are the point-by-point correlation coefficents described in the text.

A further intriguing result evident in Figures 2, 3 and 4 is that the two models including texture inheritance (starting with a 'pre-textured' aggregate at the first crossing the phase boundary, or starting with a post-perovskite aggregate with a uniform random CPO) are virtually indistinguishable 75 km above the CMB. This indicates that in our models any texture generated by the bridgmanite to post-perovskite phase transition is lost by deformation as the material moves downwards through the post-perovskite stability field. This process is illustrated for one pathline in Figure 7, where the variation in predicted anisotropy with depth and an analysis of the strain rate is shown. As the pathline approaches the CMB the strain rate increases and changes from deformation characterised by subsimple shear to deformation characterised by uniaxial compression but with increased vorticity. At the same time and at $\sim$145 km above the CMB ($r \approx 3625$ km) V_{SH} begins to rapidly increase relative to V_{SV} and the predicted anisotropy becomes indistinguishable. In order to further investigate this effect on the global pattern of anisotropy, we also evaluated the two sets of topotaxy models 175 km above the CMB, which is closer to the phase transition for much of the mantle. As shown for the P001 model in Figure 8, the shorter path lengths in the post-perovskite field at this depth mean that the two models preserve some key differences. For example, under much of China and south-east Asia, where flow is downward and the model is evaluated just inside the post-perovskite stability field, all tomography models including pre-texturing yield V_{SV} fast, while the corresponding models starting from a uniform post-perovskite texture are close to isotropic. A similar effect is seen beneath a broad band tracking south from

the western Atlantic, through the Caribbean and through South America. However, in some regions with a thicker layer of post-perovskite the texture generated by deformation inside the post-perovskite field dominates and the differences between deformation models is much larger than the differences between starting conditions. A good example of this is found off the west coast of north America, where deformation and the creation of strong anisotropy in the post-perovskite field dominates and both models give a strong V_{SH} fast signal.

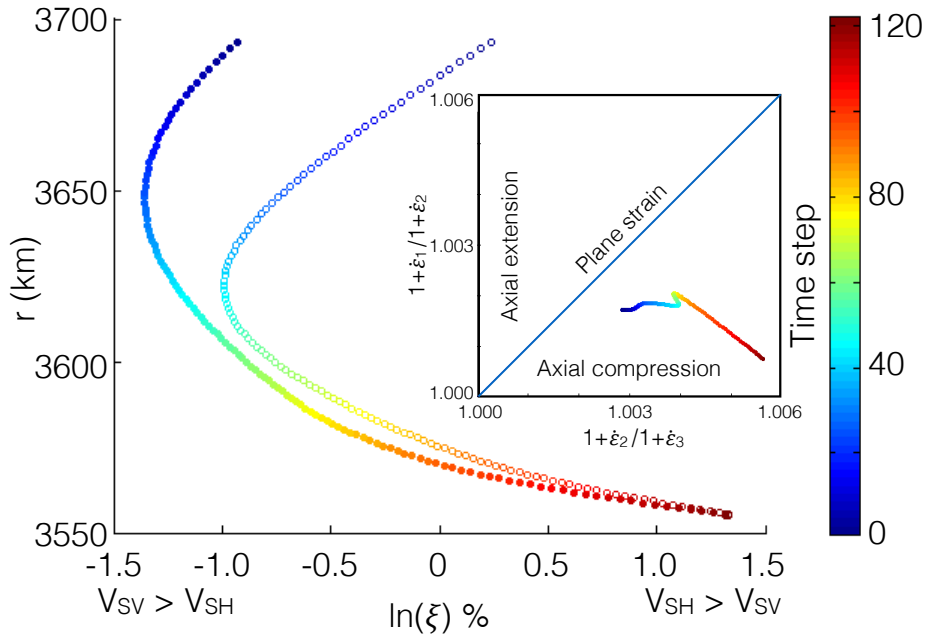

Fig. 7. Predicted seismic anisotropy along a pathline inside the post-perovskite stability field ending at 30°N 90°W and 75 km above the CMB. Filled circles represent the anisotropy when texture is inherited during the bridgmanite to post-perovskite phase transition and open circles represent the case when the initial texture is represented by 500 post-perovskite crystals drawn from a uniform random distribution (the slight positive anisotropy in this case is due to the limited number of grains included in the calculation). The colours represent the time step along the pathline (each representing 25 kyear) from the point where the pathline first crosses the phase boundary (blue, 215 km above the CMB at approximately 26°N and 84°W) to the point 122 time steps later where the particle arrives 75 km above the CMB. The inset graph shows the evolution of the strain rate tensor along the same pathline. Points represent ratios of the eigenvalues of the strain rate tensor such that plane strain plots along the diagonal with axial compression and extension plotting towards the axes. Time step is represented using the same colours as in the main figure. For all points the vorticity number is less than 1 (representing simple shear) and it increases from ∼0.5 at the start of the pathline to ∼0.7 as the pathline approaches the CMB.

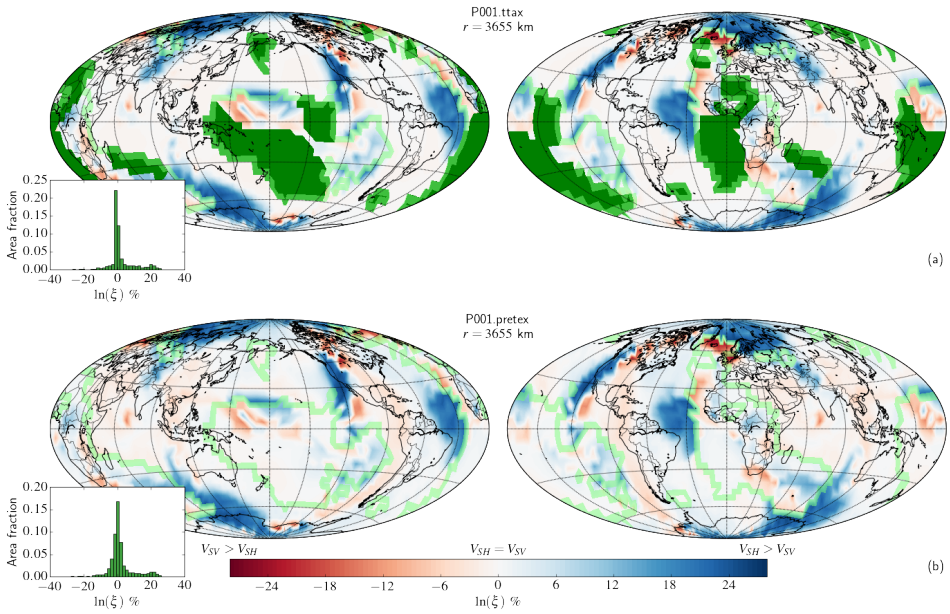

Fig. 8. Same as Figure 4 but evaluated 175 km above the CMB. The reference model from Walker et al. (2011) is not shown because this is in the isotropic perovskite field at this depth. (a) Mixed post-perovskite and bridgmanite with texture inheritance during the phase transition but starting from an isotropic post-perovskite aggregate. (b) Mixed post-perovskite and bridgmanite with texture inheritance and the development of texture during deformation in the lower mantle prior to the first bridgmanite to post-perovskite phase transition.

4 Discussion

Our results show that the inclusion of texture inheritance in models of the flow induced generation of CPO in D″ can yield patterns of seismic anisotropy that better correlate with long-wavelength patterns found from anisotropic seismic tomography than models which do not include this effect. This finding supports the hypothesis of Dobson et al. (2013), who suggested that the long-wavelength pattern of seismic anisotropy may be due to texture inheritance through the phase transition. However, even given the lack of consensus between the tomographic models, the agreement between tomography and our model of anisotropy is far from perfect. Consideration of the likely influences of the approximations and assumptions built into our modelling could provide valuable insight for future studies of D″ anisotropy. Our first assumption is that the pattern of flow in the lower mantle is known and is suitable for the prediction of strain along pathlines. A comparison of anisotropy predicted from four flow models derived from different viscosity models and the joint inversions of Simmons et al. (2007) and Simmons et al. (2009) was described by Walker et al. (2011), who showed that the differences between these models were small compared to changes due to different post-perovskite slip system parameters. However, all of these flow models were relatively smooth (the horizontal components expressed as spherical harmonics with degree 128) and

the importance of changes in flow over short distances has not been assessed. Given the difficulty in using geophysical observations to constrain flow in the deep mantle, an assessment of the importance of short length-scale features of the flow field on the global pattern of anisotropy is probably best undertaken on the basis of numerical simulations of mantle flow rather than using flow models based on geophysical inversion (although this would make direct comparison with observation more difficult). Importantly, such an approach could make the viscosity vary with temperature, or even the predicted stable phase assemblage (viscosity is only a function of depth in the approach used to derive our flow fields). Such an approach would likely complicate the pattern of flow and alter the predicted anisotropy.

A second important assumption in all our models is that all strain in the lowermost mantle is accommodated by the motion of dislocations in bridgmanite or post-perovskite. This means that our models will tend to maximise the strength of CPO and thus of the seismic anisotropy and is in contrast to some previous work. For example, Cottaar et al. (2014) include the effect of 25% periclase, which accommodates 34–40% of the strain, and cap the deformation by dislocation glide once grains have a long axis that is three times longer than the short axis. Wenk et al. (2011) use a similar procedure and assume that 50% of the strain is accommodated by deformation mechanisms such as diffusion creep, and that this does not contribute to the development of CPO. It is unlikely that all strain is accommodated by dislocation motion, but the fraction is probably stress and temperature dependent, and is unconstrained by experiment or theory in lowermost mantle phases (although recent work on bridgmanite analogues by Wang et al., 2013 and Kaercher et al., 2016 represents a step in this direction). One approach would be to attempt to tune the partitioning of strain between dislocation glide and other "invisible" mechanisms such that the strength of the anisotropy in models matches that in the observations. However, this neglects other reasons for an over-prediction of the strength of anisotropy in our models, such as the choice of the relative strength of the different slip systems (Hunt et al., 2016) or the smooth nature of the flow field, and neglects any decrease in the strength of VTI anisotropy due to the tomographic process. One area that is understudied in this regard is the importance of representing the lowermost mantle, which is presumably generally anisotropic with 21 independent elastic constants, as a VTI medium. In our comparison we assume equal azimuthal coverage but a more rigorous comparison, making use of the same ray paths as used in a particular tomographic inversion and the elastic constants from the SI, may be illuminating. With this in mind, the recent finite-frequency simulation of shear wave splitting undertaken by Nowacki and Wookey (2016) is relevant as this showed that complexity of elastic anisotropy predicted by a smooth flow field, such as that used here, gives an anisotropic response that is sometimes significantly different to that predicted by a ray theoretical approximation (e.g. Nowacki et al., 2013). In particular, the amount of splitting predicted by the finite frequency approach is typically smaller than that predicted by

the ray theoretical approximation. Such differences are likely to be even more important if a more complex flow field was used, and this produced a more rapidly varying pattern of anisotropy.

A key feature of our model is the role played by the bridgmanite to post-perovskite phase transition, but the location of this is highly uncertain. The first reason for this is that our knowledge of the location of the phase boundary in pressure-temperature space is limited and there is scatter in both experimental and computational estimates of the Clapeyron slope, and the zero K transition pressure (e.g. Hirose, 2006; Catalli et al., 2009). There is also evidence that the phase boundary moves significantly due to changes in chemistry (see Murakami et al., 2005; Grocholski et al., 2012). These problems are amplified by our approximation to the temperature structure of D″, probably one of the most difficult geophysical parameters to resolve. The joint inversion provides a map of the lateral temperature variations used (together with an estimate of the variation in compositional density) to produce the density field that drives mantle flow. We then apply these variations to a 1D geotherm to give a map of absolute temperature, which we use to predict phase stability. For compatibility with our early work (Walker et al., 2011; Ammann et al., 2014) we make use of the same choice of geotherm, Clapeyron slope, and zero K transition pressure but we note that small changes in any of these yield large variations in the area occupied by post-perovskite. In principal one could optimise the match between our model and tomography by altering the temperature field or phase stability behaviour (and observation of the switch in the sign of the anisotropy could be used as a method to map post-perovskite stability and thus temperature in the lowermost mantle) but the trade-off between the temperature and phase transition parameters would be significant. It may also be necessary to incorporate the effect of chemical variation in the lowermost mantle on the stability of post-perovskite and this would further complicate attempts in this direction. It is also worth noting that the switch in the sign of anisotropy does not always coincide with the phase transition (e.g. around the northern boundary under the Indian ocean in Figure 4), which is because pathlines leading to points within the bridgmanite stability field do not necessarily cross the closest phase boundary from the post-perovskite region. This is an illustration of the general rule that the predicted anisotropy depends on the strain along the whole of the pathline, and not just the temperature and flow pattern at a point where it is observed.

5 Conclusions

Our models lend support to the hypothesis that the long-wavelength pattern of seismic anisotropy may be due to texture inheritance through the post-perovskite to bridgmanite phase transition. In particular the best agreement between our models and anisotropic tomography are for models that invoke: (a) dislocation motion in post-perovskite dominated by glide on (001),

as suggested by the experiments of Miyagi et al. (2010); followed by (b) texture inheritance with 100% "memory" where the orientation of all post-perovskite and bridgmanite crystals are related via the relations found by Dobson et al. (2013). The correlation between our models, which do not make use of anisotropic tomography in their creation, and the tomographic results may highlight the importance of these two processes. Because of the large sensitivity to the phase boundary and anisotropy to thermal structure of the lowermost mantle (and the thermodynamics of the bridgmaite to post-perovskite phase transition) it seems feasible to use the switch in anisotropy to partially map out the temperature structure of D″, but complications due to chemical variation in the lowermost mantle may make this difficult. Importantly, the switch in sign of anisotropy in our models does not always coincide with the location of the phase boundary. This is due to the nature of CPO generation by the accumulation of strain in a flow field which leads to adjacent points being at the end of pathlines which arrive from different directions and have experienced different strain histories. Furthermore, the variation in anisotropy with height above the CMB is significant in our models and high resolution determination of the depth dependent anisotropy in the lowermost mantle may place an important constraint on the mechanism of anisotropy generation.

6 Acknowledgments

The research leading to this publication has received funding from the European Research Council under the European Union's Seventh Framework Programme (FP7/2007-2013) / ERC Grant agreement 240273 "CoMITAC" and the UK Natural Environment Research Council (NE/J009520/1). AMW acknowledges an Independent Research Fellowship from the Natural Environment Research Council (NE/K008803/1). AN is supported by a Leverhulme Early Career Fellowship. We thank Carlos Tomé and Ricardo Lebensohn for making their VPSC code available to us and two anonymous referees for useful reviews.

References

Ammann, M. W., Brodholt, J. P., Wookey, J., Dobson, D. P., 2010. First-principles constraints on diffusion in lower-mantle minerals and a weak D″ layer. Nature 465, 462 – 465.

Ammann, M. W., Walker, A. M., Stackhouse, S., Forte, A. M., Wookey, J., Brodholt, J. P., Dobson, D. P., 2014. Variation of thermal conductivity and heat flux at the earth's core mantle boundary. Earth and Planetary Science Letters 390, 175 – 185.

Beghein, C., Trampert, J., van Heijst, H. J., 2006. Radial anisotropy in seismic reference models of the mantle. Journal of Geophysical Research 111, B02303.

Caracas, R., Cohen, R. E., 2005. Effect of chemistry on the stability and elasticity of the perovskite and post-perovskite phases in the $MgSiO_3$-$FeSiO_3$-Al_2O_3 system and implications for the lowermost mantle. Geophysical Research Letters 32, L16310.

Carrez, P., Ferré, D., Cordier, P., 2007a. Implications for plastic flow in the deep mantle from modelling dislocations in $MgSiO_3$ minerals. Nature 446, 68 – 70.

Carrez, P., Ferré, D., Cordier, P., 2007b. Peierls-Nabarro model for dislocations in $MgSiO_3$ post-perovskite calculated at 120 GPa from first principles. Philosophical Magazine 87, 3229 – 3247.

Catalli, K., Shim, S.-H., Prakapenka, V., 2009. Thickness and Clapeyron slope of the post-perovskite boundary. Nature 462, 782 – 785.

Cottaar, S., Li, M., McNamara, A. K., Romanowicz, B., Wenk, H.-R., 2014. Synthetic seismic anisotropy models within a slab impinging on the core–mantle boundary. Geophysical Journal International 199, 164 – 177.

de Wit, R. W. L., Trampert, J., 2015. Robust constraints on average radial lower mantle anisotropy and consequences for composition and texture. Earth and Planetary Science Letters 429, 101 – 109.

Dobson, D. P., Hunt, S. A., Lindsay-Scott, A., Wood, I. G., 2011. Towards better analogues for $MgSiO_3$ post-perovskite: $NaCoF_3$ and $NaNiF_3$, two new recoverable fluoride post-perovskites. Physics of the Earth and Planetary Interiors.

Dobson, D. P., McCormack, R., Hunt, S. A., Ammann, M. W., Weidner, D. J., Li, L., Wang, L., 2012. The relative strength of perovskite and post-perovskite in the system $NaCoF_3$. Mineralogical Magazine 76, 925 – 932.

Dobson, D. P., Miyajima, N., Nestola, F., Alvaro, M., Casati, N., Liebske, C., Wood, I. G., Walker, A. M., 2013. Strong inheritance of texture between perovskite and post-perovskite in the D″ layer. Nature Geoscience 6, 575 – 578.

Doornbos, D. J., Spiliopoulos, S., Stacey, F. D., 1986. Seismological properties of D″ and the structure of a thermal boundary layer. Physics of the Earth and Planetary Interiors 41, 225 – 239.

Eckhardt, D. H., 1984. Correlations between global features of terrestrial fields. Mathematical Geology 16, 155 – 171.

Ford, H. A., Long, M. D., He, X., Lynner, C., 2015. Lowermost mantle flow at the eastern edge of the African Large Low Shear Velocity Province. Earth and Planetary Science Letters 420, 12 – 22.

Forte, A. M., Quéré, S., Moucha, R., Simmons, N. A., Grand, S. P., Mitrovica, J. X., Rowley, D. B., 2010. Joint seismic–geodynamic-mineral physical modelling of african geodynamics: A reconciliation of deep-mantle convection with surface geophysical constraint. Earth and Planetary Science Letters 295, 329 – 341.

Forte, A. M., Simmons, N. A., Grand, S. P., 2015. Constraints on seismic models from other disciplines - constraints on 3-D seismic models from global geodynamic observables: Implications for the global mantle convective flow.

In: Romanowicz, B., Dziewonski, A. (Eds.), Treatise of Geophysics, 2nd Edition. Vol. 1. Elsevier, Ch. 1.27, pp. 853 – 907.

French, S. W., Romanowicz, B., 2015. Broad plumes rooted at the base of the earth's mantle beneath major hotspots. Nature 525, 95 – 99.

French, S. W., Romanowicz, B. A., 2014. Whole-mantle radially anisotropic shear velocity structure from spectral-element waveform tomography. Geophysical Journal International 199, 1303 – 1327.

Garnero, E. J., McNamara, A. K., Shim, S.-H., 2016. Continent-sized anomalous zones with low seismic velocity at the base of Earth's mantle. Nature Geoscience 9, 481 – 489.

Goryaeva, A. M., Carrez, P., Cordier, P., 2015a. Modeling defects and plasticity in $MgSiO_3$ post?perovskite: Part 1—generalized stacking faults. Physics and Chemistry of Minerals 42, 781 – 792.

Goryaeva, A. M., Carrez, P., Cordier, P., 2015b. Modeling defects and plasticity in $MgSiO_3$ post?perovskite: Part 2—screw and edge [100] dislocations. Physics and Chemistry of Minerals 42, 793 – 803.

Goryaeva, A. M., Carrez, P., Cordier, P., 2016. Low viscosity and high attenuation in $MgSiO_3$ post-perovskite inferred from atomic-scale calculations. Scientific Reports 6, art. num. 34771.

Grocholski, B., Catalli, K., Shim, S.-H., Prakapenka, V., 2012. Mineralogical effects on the detectability of the postperovskite boundary. Proceedings of the National Academy of Science 109, 2275 – 2279.

Hall, S. A., Kendall, J.-M., van der Baan, M., 2004. Some comments on the effects of lower-mantle anisotropy on SKS and SKKS phases. Physics of the Earth and Planetary Interiors 146, 469 – 481.

He, X., Long, M. D., 2011. Lowermost mantle anisotropy beneath the northwestern Pacific: Evidence from PcS, ScS, SKS, and SKKS phases. Geochemistry Geophysics Geosystems 12, Q12012.

Hirose, K., 2006. Postperovskite phase transition and its geophysical implications. Reviews of Geophysics 44, RG3001.

Hirose, K., Fei, Y., Merkel, S., Ohishi, Y., 2010. Deformation of $MnGeO_3$ postperovskite at lower mantle pressure and temperature. Geophysical Research Letters 37, 1 – 5.

Hirose, K., Takafuji, N., Sata, N., Ohishi, Y., 2005. Phase transition and density of subducted morb crust in the lower mantle. Earth and Planetary Science Letters 237, 239 – 251.

Hunt, S. A., Walker, A. M., Mariani, E., 2016. *In-situ* measurement of texture development rate in $CaIrO_3$ post-perovskite. Physics of the Earth and Planetary Interiors 257, 91 – 104.

Hunt, S. A., Weidner, D. J., Li, L., Wang, L., Walte, N. P., Brodholt, J. P., Dobson, D. P., 2009. Weakening of calcium iridate during its transformation from perovskite to post-perovskite. Nature Geoscience 2, 794 – 797.

Iitaka, T., Hirose, K., Kawamura, K., Murakami, M., 2004. The elasticity of the $MgSiO_3$ post-perovskite phase in the Earth's lowermost mantle. Nature 430, 442 – 445.

Kaercher, P., Miyagi, L., Kanitoanyacharoen, W., Zepeda-Alarcon, E., Wang, Y., Parkinson, D., Lebensohn, R. A., De Carlo, F., Wenk, H.-R., 2016. Two-phase deformation of lower mantle mineral analogs. Earth and Planetary Science Letters 456, 134 – 145.

Karato, S.-I., 1998a. Seismic anisotropy in the deep mantle, boundary layers and the geometry of mantle convection. Pure and Applied Geophysics 151, 565 – 587.

Karato, S.-i., 1998b. Some remarks on the origin of seismic anisotropy in the D″ layer. Earth Planets Space 50, 1019 – 1028.

Kendall, J.-M., Silver, P. G., 1996. Constraints from seismic anisotropy on the nature of the lowermost mantle. Nature 381, 409 – 412.

Kraych, A., Carrez, P., Cordier, P., 2016a. On dislocation glide in $MgSiO_3$ bridgmanite at high-pressure and high-temperature. Earth and Planetary Science Letters 452, 60 – 98.

Kraych, A., Carrez, P., Hirel, P., Clouet, E., Cordier, P., 2016b. Peierls potential and kink-pair mechanism in high-pressure $MgSiO_3$ perovskite: An atomic scale study. Physical Review B 93, 014103.

Kustowski, B., Ekström, G., Dziewoński, 2008. Anisotropic shear-wave velocity structure of the Earth's mantle: a global model. Journal of Geophysical Research 113, B06306.

Lay, T., Garnero, E. J., 2007. Reconciling the post-perovskite phase with seismological observations of lowermost mantle structure. In: Hirose, K., Brodholt, J. P., Lay, T., Yuen, D. A. (Eds.), Post-perovskite - The last mantle phase transition. Vol. 174 of Geophysical Monograph Series. American Geophysical Union, pp. 129 – 253.

Lay, T., Hernlund, J., Buffett, B. A., 2008. Core-mantle boundary heat flow. Nature Geoscience 1, 25 – 32.

Lay, T., Young, C. J., 1991. Analysis of seismic SV waves in the core's penumbra. Geophysical Research Letters 18, 1373–1376.

Lebensohn, R. A., Tomé, C. N., 1993. A self-consistent anisotropic approach for the simulation of plastic deformation and texture development of polycrystals: Application to zirconium alloys. Acta Metallurgica et Materialia 41, 2611 – 2624.

Lekić, V., Cottaar, S., Dziewonski, A., Romanowicz, B., 2012. Cluster analysis of global lower mantle tomography: A new class of structure and implications for chemical heterogeneity. Earth and Planetary Science Letters 357-358, 68–77.

Long, M. D., 2009. Complex anisotropy in D″ beneath the eastern Pacific from SKS–SKKS splitting discrepancies. Earth and Planetary Science Letters 283, 181 – 189.

Long, M. D., Becker, T. W., 2010. Mantle dynamics and seismic anisotropy. Earth and Planetary Science Letters 297, 341 – 354.

Mainprice, D., Tommasi, A., Ferré, D., Carrez, P., Cordier, P., 2008. Predicted glide systems and crystal preferred orientations of polycrystalline silicate Mg-perovskite at high pressure: Implications for the seismic anisotropy in

the lower mantle. Earth and Planetary Science Letters, 135 – 144.

Mao, W. L., Meng, Y., Mao, H., 2010. Elastic anisotropy of ferromagnesian post-perovskite in earth's d" layer. Physics of the Earth and Planetary Interiors 180, 203 – 208.

McCormack, R., Dobson, D. P., Walte, N. P., Miyajima, N., Taniguchi, T., Wood, I. G., 2011. The development of shape- and crystallographic-preferred orientation in $CaPtO_3$ post-perovskite deformed in pure shear. American Mineralogist 96, 1630 – 1635.

McNamara, A. K., van Keken, P. E., Karato, S.-I., 2002. Development of anisotropic structure in the Earth's lower mantle by solid-state convection. Nature 416, 310 – 314.

Merkel, S., Kubo, A., Miyagi, L., Speziale, S., Duffy, T. S., Mao, H., Wenk, H.-R., 2006. Plastic deformation of $MgGeO_3$ post-perovskite at lower mantle pressures. Science 311, 644 – 646.

Merkel, S., McNamara, A. K., Kubo, A., Speziale, S., Miyagi, L., Meng, Y., Duffy, T. S., Wenk, H.-R., 2007. Deformation of (Mg,Fe)SiO_3 post-perovskite and D" anisotropy. Science 316, 1729 – 1732.

Metsue, A., Carrez, P., Mainprice, D., Cordier, P., 2009. Numerical modelling of dislocations and deformation mechanisms in $CaIrO_3$ and $MgGeO_3$ post-perovskites — Comparison with $MgSiO_3$ post-perovskite. Physics of the Earth and Planetary Interiors 174, 165 – 173.

Metsue, A., Tsuchiya, T., 2013. Shear response of Fe-bearing $MgSiO_3$ post-perovskite at lower mantle pressures. Proceedings of the Japan Academy Series B, Physical and Biological Sciences 89, 51 – 58.

Miyagi, L., Kanitpanyacharoen, W., Kaercher, P., Lee, K. K. M., Wenk, H.-R., 2010. Slip systems in $MgSiO_3$ post-perovskite: implications for D″ anisotropy. Science 329, 1636 – 1638.

Miyagi, L., Kanitpanyacharoen, W., Stackhouse, S., Militzer, B., Wenk, H.-R., 2011. The enigma of post-perovskite anisotropy: deformation versus transformation textures. Physics and Chemistry of Minerals 38, 665 – 678.

Miyagi, L., Nishiyama, N., Wang, Y., Kubo, A., West, D. V., Cava, R. J., Duffy, T. S., Wenk, H.-R., 2008. Deformation and texture development in $CaIrO_3$ post-perovskite phase up to 6 GPa and 1300 K. Earth and Planetary Science Letters 268, 515 – 525.

Miyajma, N., Walte, N., 2009. Burgers vector determination in deformed perovskite and post-perovskite of $CaIrO_3$ using thickness fringes in weak-beam dark-field images. Ultramicroscopy 109, 683 – 692.

Montagner, J.-P., Kennett, B. L. N., 1996. How to reconcile body-wave and normal-mode reference Earth models. Geophysical Journal International 125, 229 – 248.

Moulik, P., Ekström, G., 2014. An anisotropic shear velocity model of the earth's mantle using normal modes, body waves, surface waves and long-period waveforms. Geophysical Journal International 199, 1713 – 1738.

Murakami, M., Hirose, K., Kawamura, K., Sata, N., Ohishi, Y., 2004. Post-perovskite phase transition in $MgSiO_3$. Science 304, 855 – 858.

Murakami, M., Hirose, K., Sata, N., Ohishi, Y., 2005. Post-perovskite phase transition and mineral chemistry in the pyrolitic lowermost mantle. Geophysical Research Letters 32, L03304.

Murakami, M., Sinogeikin, S. V., Bass, J. D., Sata, N., Ohishi, Y., Hirose, K., 2007. Sound velocity of $MgSiO_3$ post-perovskite phase: A constraint on the D'' discontinuity. Earth and Planetary Science Letters 259, 18 – 23.

Nisr, C., Ribárik, G., Ungár, T., Vaughan, G. B. M., Cordier, P., Merkel, S., 2012. High resolution three-dimensional X-ray diffraction study of dislocations in grains of $MgGeO_3$ post-perovskite at 90 GPa. Journal of Geophysical Research 117, B03201.

Niwa, K., Yagi, T., Ohgushi, K., Merkel, S., Miyajma, N., Kikegawa, T., 2007. Lattice preferred orientation in $CaIrO_3$ perovskite and post-perovskite formed by plastic deformation under pressure. Physics and Chemistry of Minerals 34, 679 – 686.

Nowacki, A., Walker, A. M., Wookey, J., Kendall, J.-M., 2013. Evaluating post-perovskite as a cause of D$''$ anisotropy in regions of palaeosubduction. Geophysical Journal International 192, 1085 – 1090.

Nowacki, A., Wookey, J., 2016. The limits of ray theory when measuring shear wave splitting in the lowermost mantle with ScS waves. Geophysical Journal International TBC.

Nowacki, A., Wookey, J., Kendall, J.-M., 2010. Deformation of the lowermost mantle from seismic anisotropy. Nature 467, 1091 – 1094.

Nowacki, A., Wookey, J., Kendall, J.-M., 2011. New advances in using seismic anisotropy, mineral physics and geodynamics to understand deformation in the lowermost mantle. Journal of Geodynamics 52, 205 – 228.

Oganov, A. R., Brodholt, J. P., Price, G. D., 2001. Ab initio elasticity and thermal equation of state of $MgSiO_3$ perovskite. Earth and Planetary Science Letters 184, 555 – 560.

Oganov, A. R., Martoňák, R., Laio, A., Raiteri, P., Parrinello, M., 2005. Anisotropy of Earth's D$''$ layer and stacking faults in the $MgSiO_3$ post-perovskite phase. Nature 438, 1142 – 1144.

Oganov, A. R., Ono, S., 2004. Theoretical and experimental evidence for a post-perovskite phase of $MgSiO_3$ in Earth's D$''$ layer. Nature 430, 445 – 448.

Okada, T., Yagi, T., Niwa, K., Kikegawa, T., 2010. Lattice-preferred orientations in post-perovskite-type $MgGeO_3$ formed by transformations from different pre-phases. Physics of the Earth and Planetary Interiors 180, 195 – 202.

Panning, M., Romanowicz, B., 2004. Inferences on flow at the base of Earth's mantle based on seismic anisotropy. Science 303, 351 – 353.

Panning, M., Romanowicz, B., 2006. A three-dimensional radially anisotropic model of shear velocity in the whole mantle. Geophysical Journal International 167, 361 – 379.

Panning, M. P., Lekić, V., Romanowicz, B. A., 2010. Importance of crustal corrections in the development of a new global model of radial anisotropy.

Journal of Geophysical Research 115, B12325.
Ray, T. W., Anderson, D. L., 1994. Spherical disharmonies in the earth sciences and the spatial solution: Ridges, hotspots, slabs, geochemistry and tomography correlations. Journal of Geophysical Research 99, 9605 – 9614.
Rokosky, J. M., Lay, T., Garnero, E. J., 2006. Small-scale lateral variations in azimuthally anisotropic D″ structure beneath the Cocos Plate. Earth and Planetary Science Letters 248, 411 – 425.
Simmons, N. A., Forte, A. M., Grand, S. P., 2007. Thermochemical structure and dynamics of the African superplume. Geophysical Research Letters 34, L02301.
Simmons, N. A., Forte, A. M., Grand, S. P., 2009. Joint seismic, geodynamic and mineral physical constraints on three-dimensional mantle heterogeneity: Implications for the relative importance of thermal versus compositional heterogeneity. Geophysical Journal International 177, 1284 – 1304.
Stacey, F. D., Davis, P. M., 2008. Physics of the Earth, 4th Edition. Cambridge University Press.
Stackhouse, S., Brodholt, J. P., 2007. The high temperature elasticity of $MgSiO_3$ post-perovskite. In: Hirose, K., Brodholt, J., Lay, T., Yuen, D. (Eds.), Geophysical Monograph: Post-Perovskite - The Last Mantle Phase Transition. Vol. 174 of Geophysical Monograph Series. AGU, pp. 99 – 113.
Stackhouse, S., Brodholt, J. P., Wookey, J., Kendall, J.-M., Price, G. D., 2005. The effect of temperature on the seismic anisotropy of the perovskite and post-perovskite polymorphs of $MgSiO_3$. Earth and Planetary Science Letters 230, 1 – 10.
Thomas, C., Wookey, J., Brodholt, J., Fieseler, T., 2011. Anisotropy as cause for polarity reversals of D″ reflections. Earth and Planetary Science Letters 307, 369 – 376.
Tschauner, O., Kiefer, B., Liu, H., Sinogeikin, S., Somayazulu, M., Luo, S.-N., 2008. Possible structural polymorphism in al-bearing magnesiumsilicate post-perovskite?. American Mineralogist 93, 533 – 539.
Tsuchiya, T., Tsuchiya, J., Umemoto, K., Wentzcovitch, 2004a. Phase transition in $MgSiO_3$ perovskite in the Earth's lower mantle. Earth and Planetary Science Letters 224, 241 – 248.
Tsuchiya, T., Tsuchiya, J., Umemoto, K., Wentzcovitch, R. M., 2004b. Elasticity of post-perovskite $MgSiO_3$. Geophysical Research Letters 31, L14603.
Tsujino, N., Nishihara, Y., Yamazaki, D., Seto, Y., Higo, Y., Takahashi, E., 2016. Mantle dynamics inferred from the crystallographic preferred orientation of bridgmanite. Nature 539, 81 – 84.
Vinnik, L., Romanowicz, B., Le Stunff, Y., Makeyeva, L., 1995. Seismic anisotropy in the D″ layer. Geophysical Research Letters 22, 1657 – 1660.
Walker, A. M., Forte, A. M., Wookey, J., Nowacki, A., Kendall, J.-M., 2011. Elastic anisotropy of D″ predicted from global models of mantle flow. Geochemistry Geophysics Geosystems 12, Q10006.
Walker, A. M., Wookey, J., 2012. MSAT – a new toolkit for the analysis of elastic and seismic anisotropy. Computers and Geosciences 49, 81 – 90.

Walte, N., Heidelbach, F., Miyajma, N., Frost, D., 2007. Texture development and TEM analysis of deformed $CaIrO_3$: Implications for the D″ layer at the core-mantle boundary. Geophysical Research Letters 34, L08306.

Walte, N. P., Heidelbach, F., Miyajma, N., Frost, D. J., Rubie, D. C., Dobson, D. P., 2009. Transformation textures in post-perovskite: Understanding mantle flow in the D″ layer of the Earth. Geophysical Research Letters 36, L04302.

Wang, Y., Hilairet, N., Nishiyama, N., Yahata, N., Tsuchiya, T., Morard, G., Fiquet, G., 2013. High-pressure, high-temperature deformation of $CaGeO_3$ (perovskite)±MgO aggregates: Implications for multiphase rheology of the lower mantle. Geochemistry Geophysics Geosystems 14, 3389 – 3408.

Wenk, H.-R., Cottaar, S., Tomé, C. N., McNamara, A., Romanowicz, B., 2011. Deformation in the lowermost mantle: From polycrystal plasticity to seismic anisotropy. Earth and Planetary Science Letters 306, 33 – 45.

Wenk, H.-R., Speziale, S., McNamara, A. K., Garnero, E. J., 2006. Modeling lower mantle anisotropy development in a subducting slab. Earth and Planetary Science Letters 245, 302 – 314.

Wentzcovitch, R. M., Karki, B. B., Cococcioni, M., de Gironcoli, S., 2004. Thermoelastic properties of $MgSiO_3$-perovskite: Insights on the nature of the Earth's lower mantle. Physical Review Letters 92.

Wentzcovitch, R. M., Tsuchiya, T., Tsuchiya, J., 2006. $MgSiO_3$ postperovskite at D″ conditions. Proceedings of the National Academy of Science 103, 543 – 546.

Wookey, J., Kendall, J.-M., 2007. Seismic anisotropy of post-perovskite and the lowermost mantle. In: Hirose, K., Brodholt, J., Lay, T., Yuen, D. (Eds.), Post-perovskite: the last mantle phase transition. Vol. 174 of Geophysical Monograph Series. AGU, pp. 171 – 189.

Wookey, J., Kendall, J.-M., 2008. Constraints on lowermost mantle mineralogy and fabric beneath Siberia from seismic anisotropy. Earth and Planetary Science Letters 275, 32 – 42.

Wookey, J., Kendall, J.-M., Rümpker, G., 2005a. Lowermost mantle anisotropy beneath the north Pacific from differential *S*–*ScS* splitting. Geophysical Journal International 161, 829 – 838.

Wookey, J., Stackhouse, S., Kendall, J.-M., Brodholt, J. P., Price, G. D., 2005b. Efficacy of the post-perovskite phase as an explanation for lowermost-mantle seismic properties. Nature 438, 1004 – 1007.

Yamazaki, D., Yoshino, T., Ohfuji, H., Ando, J., Yoneda, A., 2006. Origin of seismic anisotropy in the D″ layer inferred from shear deformation experiments on post-perovskite phase. Earth and Planetary Science Letters 252, 372 – 378.

Zahn, D., 2011. Shearing mechanisms of $MgSiO_3$ at conditions of the Earth's D″ layer. Geophysical Research Letters 38, L16319.

Zahn, D., 2013. Nucleation mechanism and kinetics of the perovskite to post-perovskite transition of $MgSiO_3$ under extreme conditions. Chemical Physics Letters 573, 5 – 7.